PREDICTION OF MEAN AND TURBULENT KINETIC ENERGY IN RECTANGULAR SHALLOW RESERVOIRS

ERICA CAMNASIO, Researcher, Politecnico di Milano, Department of Civil and Environmental Engineering (D.I.C.A.), piazza Leonardo da Vinci, 32, 20133 Milano, Italy. E-mail: erica.camnasio@polimi.it

SEBASTIEN ERPICUM, Laboratory Manager, University of Liège (ULg), ArGEnCo department, Research group Hydraulics in Environmental and Civil Engineering (HECE), Chemin des Chevreuils, 1, Bat B52/3, 4000 Liège, Belgium. E-mail: s.erpicum@ulg.ac.be

PIERRE ARCHAMBEAU, Research Associate, University of Liège (ULg), ArGEnCo department, Research group Hydraulics in Environmental and Civil Engineering (HECE), Chemin des Chevreuils, 1, Bat B52/3, 4000 Liège, Belgium. E-mail: pierre.archambeau@ulg.ac.be

MICHEL PIROTTON, Professor, University of Liège (ULg), ArGEnCo department, Research group Hydraulics in Environmental and Civil Engineering (HECE), Chemin des Chevreuils, 1, Bat B52/3, 4000 Liège, Belgium. E-mail: michel.pirotton@ulg.ac.be

BENJAMIN DEWALS (**author for correspondence. tel. +32 (0)4 3669283**), Assistant Professor, University of Liège (ULg), ArGEnCo Department, Research group Hydraulics in Environmental and Civil Engineering (HECE), Chemin des Chevreuils, 1, Bat B52/3, 4000 Liège, Belgium. Email: b.dewals@ulg.ac.be

ABSTRACT

Shallow rectangular reservoirs are common structures in urban hydraulics and river engineering. Despite their simple geometry, complex symmetric and asymmetric flow fields develop in such reservoirs, depending on their expansion ratio and length-to-width ratio.

The original contribution of this study is the analysis of the kinetic energy content of the mean flow, based on UVP velocity measurements carried throughout the reservoir in eleven different geometric configurations. A new relationship is derived between the specific mean kinetic energy and the reservoir shape factor.

For most considered geometric configurations, leading to four different flow patterns, the experimentally observed flow fields and mean kinetic energy contents are successfully reproduced by an operational numerical model based on the depth-averaged flow equations and a two-length-scale k-ε turbulence closure. The analysis also highlights the better performance of this depth-averaged k-ε model compared to an algebraic turbulence model.

Finally, the turbulent kinetic energy in the reservoir is derived from the experimental measurements and the corresponding numerical predictions based on the k-ε model agree satisfactorily in the main jet but not in the recirculation zones.

Keywords: shallow reservoir, turbulent kinetic energy, UVP measurements, flow fields.

1. INTRODUCTION

Rectangular shallow reservoirs are structures commonly used in urban hydraulics and river engineering. The capacity of these reservoirs varies from a few hundred cubic meters for small urban drainage structures up to millions of cubic meters for large fluvial schemes. They may serve either as retention basins to protect against flooding or as settling basins to trap polluted or sediment material (e.g., Chau and Jiang, 2004; Wu and Chau, 2006). In the former case, deposition should be minimized, while it must be maximized in the latter case. Therefore, predicting the amount and location of deposits is essential, both for the design and the optimal operation of such reservoirs. The geometric configuration of rectangular shallow reservoirs may also be regarded as a useful idealization of more complex situations, such as river-floodplain systems (Chu et al., 2004) or applications in different fields of chemical, civil and environmental engineering (Goula et al., 2008; Lee et al., 2013; Ng and Chau 2014).

Dufresne et al. (2009; 2010a) showed that the pattern of sediment deposits highly depends on the complex flow fields developing in such reservoirs, as highlighted by recent experimental research (Camnasio et al., 2011; Camnasio et al., 2013; Dewals et al., 2008; Dufresne et al., 2012). Besides a symmetric flow with a central jet (patterns S0 and S1), several asymmetric flow patterns were identified, despite the hydraulic and geometric symmetry of the experimental setups (Figure 1). In particular, the observed flow patterns are characterized by one or two reattachment points (respectively, A1 and A2 patterns).

A typology of turbulent flow patterns in shallow rectangular reservoirs was given by Dufresne et al. (2010b) as a function of the non-dimensional length of the reservoir $L / \Delta B$ and its expansion ratio $\Delta B / b$, where L is the reservoir length, ΔB the lateral expansion and b the width of the channels at the outlet and inlet of the reservoir. It was shown that the transition between symmetric and asymmetric flow patterns is controlled by the shape factor $S = L / \Delta B^{0.6} / b^{0.4}$.

64 The experimentally observed flow patterns were reproduced by numerical simulations either based
65 on the Reynolds-Averaged Navier-Stokes equations (Dufresne et al., 2009) or using more
66 operational models based on the shallow water equations (Dewals et al., 2008; Liu et al., 2010;
67 Dufresne et al., 2011). In particular, Dewals et al. (2008) presented numerical simulations based on
68 a finite volume model including a two-length-scale depth-averaged k-ε turbulence closure. Peng et
69 al. (2011) used a Lattice Boltzmann model with turbulence modelling.
70 Dufresne (2010a) showed that the trapping efficiency of shallow rectangular reservoirs rises
71 abruptly when the flow pattern changes from symmetric (S0 or S1) to asymmetric (A1 or A2) as the
72 geometry of the reservoir is varied and the shape factor S exceeds a threshold value. In this paper,
73 we investigate for the first time the influence of this shape factor S on the mean kinetic energy
74 content of the flow. In particular, combining experimental data of Camnasio et al. (2011) and new
75 numerical simulations, the authors have developed a distinct relationship between the logarithm of
76 this shape factor and the specific mean kinetic energy content of the reservoir. We also show that
77 the depth-averaged k-ε turbulence model used by Dewals et al. (2008) performs well at predicting
78 the specific mean kinetic energy content of the flow in eleven different geometric configurations.
79 Next, we present measurements of turbulent kinetic energy for the same range of reservoir
80 geometries and, using the depth-averaged k-ε model, we assess the ability of the numerical model to
81 simulate the distribution of turbulent kinetic energy throughout the basin. This is of paramount
82 importance to predict diffusion of suspended load and therefore location of sediment deposits. So
83 far, existing literature on flow in rectangular shallow reservoirs provides neither measurements of
84 turbulent kinetic energy nor corresponding numerical simulations.
85 Dewals et al. (2008) used two different turbulence closures: either an algebraic model or a two-
86 length-scale depth-averaged k-ε model (e.g., Dufresne et al., 2011). However, comparisons between
87 these turbulence closures for predicting flow in rectangular shallow reservoirs have remained
88 limited and focused solely on the A1 flow pattern (Dewals et al., 2008). Therefore, we also discuss

here a comparison of the performance of the algebraic closure and the k-ε model for all flow patterns observed experimentally.

2. LABORATORY EXPERIMENTS

2.1 Experimental setup

Experiments have been carried out in the same facility as described by Dewals et al. (2008) and Camnasio et al. (2011). It consists in a rectangular reservoir of adjustable length L and width B. Their maximum values are, respectively, 6 m and 4 m (Figure 2). The maximum water depth in the reservoir is 0.3 m. The horizontal bottom of the reservoir is smooth and made of polyvinyl chloride (PVC). The inlet and outlet of the reservoir consist of two horizontal free-surface rectangular channels, with a constant width b = 0.25 m and a length equal to 1 m. They are located along the centreline of the reservoir, on two opposite faces of the reservoir (upstream and downstream). Movable PVC walls enable changes in the length L and the width B of the reservoir, in order to test different length-to-width ratios L/B and expansion ratios $\Delta B/b$.

In the experiments presented here, the discharge Q is kept constant at the value Q = 7 l/s. By means of a tailgate located at the downstream end of the outlet channel, the water depth h in the reservoir is also maintained constant, at the value h = 0.2 m. At the reservoir inlet, these values correspond to a Reynolds number $\mathrm{Re}_{in} = 4V_{in}h/\nu = 112{,}000$ and a Froude number $\mathrm{Fr}_{in} = V_{in}/(gh)^{0.5} = 0.1$, where V_{in} is the average velocity in the inlet channel, g the gravity acceleration and ν the kinematic viscosity.

2.2 Velocity measurements

Velocity measurements have been performed using eight ultrasound velocity profilers (UVP) manufactured by Metflow (Camnasio et al., 2011). Each UVP device measures the flow velocity in one direction along a profile aligned with the instrument axis.

As depicted in Figure 3, the UVP devices were arranged along two adjacent sides of a horizontal square grid of 1 m by 1 m, enabling the measurement of the two horizontal velocity components in

the sixteen points formed by the intersections of the velocity profiles measured by each UVP device. The distance between these points was about 14 cm. This square grid could be moved all over the reservoir to obtain the flow field throughout the whole reservoir surface.

A preliminary investigation of the 2D horizontal velocity components was carried out at different heights z from the bottom (0.01, 0.06, 0.11 and 0.18 m) and at several locations in the reservoir, from which a mean velocity profile along the depth could be deduced. As a result, the subsequent velocity measurements have been performed by setting the UVP devices at a height $z = 0.4\ h = 0.08$ m in order to obtain a representative value of the depth-averaged velocity.

2.3 Experimental tests

Experiments were carried out in the following way: water was circulated in the system until water depth and discharge reached a steady state; then, the grid formed by the UVP probes was placed at its first position in the reservoir and the acquisition of velocity data was started. After the measurements, the grid was moved in the next position in the reservoir, in order to cover progressively the entire reservoir surface.

Eleven reservoir geometries have been considered, as detailed in Table 1. For a fixed aspect ratio $\Delta B / b = 7.5$, tests 1 to 5 focus on the effect of the non-dimensional length of the reservoir ($L / \Delta B = 1.6$ to 3.2) on the transition between flow patterns S0, S1 and A1. This analysis is complemented by tests 6 to 11 for non-dimensional lengths up to 34.3, but with expansion ratios varying between 0.7 and 5.5, due to constraints arising from the experimental setup. For each geometric configuration, Table 1 also provides the shape factor $S = L / \Delta B^{0.6} / b^{0.4}$ as introduced by Dufresne et al. (2010b).

3. NUMERICAL SIMULATIONS

Numerical simulations of the experimental flow configurations have been carried out with the finite volume model WOLF 2D of the University of Liege. It solves the shallow water equations on a

Cartesian grid and achieves second-order accuracy in space and time (e.g., Erpicum et al., 2010). The model is briefly presented hereafter, while Dewals et al. (2008) as well as Dufresne et al. (2011) describe in detail the application of the computational method for flow in rectangular shallow reservoirs.

3.1 Mathematical model

The shallow-water equations are used. They correspond to the Reynolds-averaged Navier-Stokes equations along the *x* and *y* directions, averaged along the water depth. Considering a horizontal bottom, they write as follows (Erpicum et al., 2009):

$$\frac{\partial hu}{\partial t}+\frac{\partial hu^2}{\partial x}+\frac{\partial huv}{\partial y}+\frac{\partial}{\partial x}\left(\frac{gh^2}{2}\right)=\frac{\tau_{bx}}{\rho}+\frac{1}{\rho}\frac{\partial h\tau_{xx}}{\partial x}+\frac{1}{\rho}\frac{\partial h\tau_{xy}}{\partial y}, \quad (1)$$

$$\frac{\partial hv}{\partial t}+\frac{\partial huv}{\partial x}+\frac{\partial hv^2}{\partial y}+\frac{\partial}{\partial y}\left(\frac{gh^2}{2}\right)=\frac{\tau_{by}}{\rho}+\frac{1}{\rho}\frac{\partial h\tau_{xy}}{\partial x}+\frac{1}{\rho}\frac{\partial h\tau_{yy}}{\partial y}, \quad (2)$$

with *t* the time, *u* and *v* the velocity components along the horizontal directions *x* and *y*. The *x*- and *y*-components of the bottom shear stress, τ_{bx} and τ_{by}, are estimated using Darcy-Weisbach formulation:

$$\frac{\tau_{bx}}{\rho}=\frac{f}{8}u\sqrt{u^2+v^2} \qquad \text{and} \qquad \frac{\tau_{by}}{\rho}=\frac{f}{8}v\sqrt{u^2+v^2}, \quad (3)$$

in which the friction coefficient *f* is given by Colebrook formula, assuming a smooth bottom.

The derivatives of the depth-averaged viscous and turbulent stresses τ_{xx}, τ_{xy} and τ_{yy} are expressed using Boussinesq's assumption formulated for a depth-averaged flow model (Erpicum et al., 2009):

$$\frac{\partial h\tau_{xx}}{\partial x}+\frac{\partial h\tau_{xy}}{\partial y}=\left(\nu+\nu_T^{3D}\right)\left(\frac{\partial^2 hu}{\partial x^2}+\frac{\partial^2 hu}{\partial y^2}\right)+\frac{\partial}{\partial x}\left[\nu_T^{2D}\left(\frac{\partial hu}{\partial x}-\frac{\partial hv}{\partial y}\right)-k'\right]+\frac{\partial}{\partial y}\left[\nu_T^{2D}\left(\frac{\partial hv}{\partial x}+\frac{\partial hu}{\partial y}\right)\right], \quad (4)$$

$$\frac{\partial h\tau_{yx}}{\partial x}+\frac{\partial h\tau_{yy}}{\partial y}=\left(\nu+\nu_T^{3D}\right)\left(\frac{\partial^2 hv}{\partial x^2}+\frac{\partial^2 hv}{\partial y^2}\right)+\frac{\partial}{\partial y}\left[\nu_T^{2D}\left(\frac{\partial hv}{\partial y}-\frac{\partial hu}{\partial x}\right)-k'\right]+\frac{\partial}{\partial x}\left[\nu_T^{2D}\left(\frac{\partial hv}{\partial x}+\frac{\partial hu}{\partial y}\right)\right], \quad (5)$$

where *k'* is the depth-integrated turbulent kinetic energy, while ν, ν_T^{3D} and ν_T^{2D} refer, respectively, to the kinematic viscosity of water, the eddy viscosity related to bed-generated turbulence and the

158 eddy viscosity related to large-scale transverse shear-generated turbulence. From a local equilibrium
159 assumption, ν_T^{3D} is given by: $\nu_T^{3D} = c_\nu h u_*$, with u_* the bottom friction velocity and $c_\nu \approx 0.08$ for
160 non-stratified flow of uniform density along the depth (Erpicum et al., 2009).

161 The two-dimensional large scale eddy viscosity $\nu_{T,2D}$ is evaluated as a function of the depth-
162 integrated turbulent kinetic energy *k'* and its rate of dissipation ε: $\nu_{T,2D} = c_\mu k'^2/\varepsilon$. These variables
163 are governed by two additional transport equations:

164
$$\frac{\partial k'}{\partial t} + \frac{\partial uk'}{\partial x} + \frac{\partial vk'}{\partial y} = \frac{\partial}{\partial x}\left(\frac{\nu + \nu_T^{3D}}{h}\frac{\partial k'h}{\partial x}\right) + \frac{\partial}{\partial y}\left(\frac{\nu + \nu_T^{3D}}{h}\frac{\partial k'h}{\partial y}\right) + \frac{\partial}{\partial x}\left[\frac{\nu_{T,2D}}{\sigma_k}\frac{\partial k'}{\partial x}\right] + \frac{\partial}{\partial y}\left[\frac{\nu_{T,2D}}{\sigma_k}\frac{\partial k'}{\partial y}\right] - k'\frac{\partial u}{\partial x} - k'\frac{\partial v}{\partial y} + P - F - \frac{\varepsilon}{h} \quad (6)$$

165
$$\frac{\partial \varepsilon}{\partial t} + \frac{\partial u\varepsilon}{\partial x} + \frac{\partial v\varepsilon}{\partial y} = \frac{\partial}{\partial x}\left(\frac{\nu + \nu_T^{3D}}{h}\frac{\partial \varepsilon h}{\partial x}\right) + \frac{\partial}{\partial y}\left(\frac{\nu + \nu_T^{3D}}{h}\frac{\partial \varepsilon h}{\partial y}\right) + \frac{\partial}{\partial x}\left[\frac{\nu_{T,2D}}{\sigma_\varepsilon}\frac{\partial \varepsilon}{\partial x}\right] + \frac{\partial}{\partial y}\left[\frac{\nu_{T,2D}}{\sigma_\varepsilon}\frac{\partial \varepsilon}{\partial y}\right] + c_{1\varepsilon}\frac{\varepsilon}{k}\left[P - (1 - c_{3\varepsilon})F\right] - c_{2\varepsilon}\frac{\varepsilon^2}{hk'} \quad (7)$$

166 The terms *P* and *F*, representing the production of the large scale horizontal turbulence and the
167 effect of wall friction are given by the following expressions:

168
$$P = \nu_{T,2D}\left[\left(\frac{\partial uh}{\partial x} - \frac{\partial vh}{\partial y}\right)\left(\frac{\partial u}{\partial x} - \frac{\partial v}{\partial y}\right) + \left(\frac{\partial uh}{\partial y} + \frac{\partial vh}{\partial x}\right)\left(\frac{\partial u}{\partial y} + \frac{\partial v}{\partial x}\right)\right], \quad (8)$$

169
$$F = \frac{f}{8h}\left[3k'\sqrt{u^2 + v^2} - \nu_{T,2D}\frac{\left(\frac{\partial hu}{\partial x} - \frac{\partial hv}{\partial y}\right)\left(u^2 - v^2\right) + 2\left(\frac{\partial hu}{\partial y} + \frac{\partial hv}{\partial x}\right)uv}{\sqrt{u^2 + v^2}}\right]. \quad (9)$$

170 The production term *P* is directly related to the gradients of horizontal velocity components and unit
171 discharges, while the term *F* contributes to dissipation of turbulence. The values of the constants
172 involved in the above equations are given following Erpicum et al. (2009) and Babarutsi and Chu
173 (1998): $c_\mu = 0.09$, $\sigma_k = 1$, $\sigma_\varepsilon = 1.3$, $c_{1\varepsilon} = 1.44$, $c_{2\varepsilon} = 1.92$ and $c_{3\varepsilon} = 0.8$.

174 The predictions of the *k*-ε turbulence model are compared with those obtained with an algebraic
175 model based on Elder formula (Fischer et al., 1979), in which the eddy viscosity is simply evaluated

as $\nu_T = \alpha h u_*$. In this model, the derivatives of the depth-averaged viscous and turbulent stresses are given by:

$$\frac{\partial h\tau_{xx}}{\partial x} + \frac{\partial h\tau_{xy}}{\partial y} = \frac{\partial}{\partial x}\left[h\left(\nu + \nu_T\right)\left(\frac{\partial u}{\partial x} - \frac{\partial v}{\partial y}\right)\right] + \frac{\partial}{\partial y}\left[h\left(\nu + \nu_T\right)\left(\frac{\partial v}{\partial x} + \frac{\partial u}{\partial y}\right)\right] \quad (10)$$

$$\frac{\partial h\tau_{yx}}{\partial x} + \frac{\partial h\tau_{yy}}{\partial y} = \frac{\partial}{\partial y}\left[h\left(\nu + \nu_T\right)\left(\frac{\partial v}{\partial y} - \frac{\partial u}{\partial x}\right)\right] + \frac{\partial}{\partial x}\left[h\left(\nu + \nu_T\right)\left(\frac{\partial v}{\partial x} + \frac{\partial u}{\partial y}\right)\right] \quad (11)$$

Parameter α represents an empirical coefficient, which was set here at $\alpha = 1$, consistently with previous research (Dewals et al., 2008).

3.2 Numerical model

The numerical model handles Cartesian grids, on which the equations detailed above are solved based on a finite volume scheme. The reconstruction of the variables is performed linearly, with slope-limitation. Unlike many shallow-water models based on Riemann solvers (e.g., Lai and Khan 2012), a flux-vector splitting (FVS) technique is used for the discretization of the advective terms. As shown by Erpicum et al. (2010), this FVS is robust, computationally efficient and Froude-independent. The diffusive and source terms are all evaluated by a centred scheme. Since the model is used here to compute steady state flows, a dissipative first order 3-step Runge-Kutta algorithm was used for the time integration.

The grid spacing used for spatial discretization is of 2.5 cm, leading to a total number of 38,800 cells in the largest reservoir configuration. A grid independence test was presented by Dufresne et al. (2011) based on the grid convergence index proposed by Roache (1994).

The time step used in the simulations is of the order of 5×10^{-3} seconds, as it is constrained by the Courant-Friedrichs-Lewy stability condition. The bottom shear stress terms are discretized semi-implicitly. This enhances the stability of the scheme, at no significant extra computational cost.

3.3 Boundary and initial conditions

In all simulations, the downstream water depth h = 0.2 m is prescribed as a boundary condition at the outlet, while the inlet boundary condition is a constant unit discharge hu = 0.028 m²/s, corresponding to a total discharge of 7 l/s. As detailed by Dewals et al. (2008; 2012), a slight transverse disturbance (~ 1 %) was introduced in the inflow profile of unit discharge. By acting as a seed for asymmetry in the simulation, this disturbed boundary condition enables to test the stability of the computed flow field with respect to small perturbations of the inflow.

At solid walls, the component of the specific discharge normal to the wall is set to zero. As regards the discretization of the diffusive terms, the gradients of the unknowns in the direction parallel to the boundary are set to zero for simplicity, while the gradients in the direction normal to the boundary are properly evaluated by finite difference between the value at the boundary and the value at the centre of the adjacent cell.

To estimate the turbulence variables at solid walls, the shear velocity is computed using to the law of the wall. The corresponding depth-integrated turbulent kinetic energy and dissipation rate are evaluated according to Erpicum et al. (2009):

$$k' = \frac{hU_\tau^2}{\sqrt{c_\mu}} \qquad \text{and} \qquad \varepsilon = \frac{h^2 U_\tau^3}{\kappa d}, \tag{12}$$

with U_τ the shear velocity assuming a logarithmic velocity profile near the wall, κ the von Karman constant and d the distance to the wall. At inlets, the depth-integrated turbulent kinetic energy and its dissipation rate are set as follows (Choi and Garcia, 2002):

$$k' = 10^{-4} hu^2 \qquad \text{and} \qquad \varepsilon = 10 \frac{k^{3/2}}{\sqrt{h}}. \tag{13}$$

All the numerical simulations were repeated twice, starting from two different initial conditions, corresponding respectively to water at rest (i.e., symmetric) and to an asymmetric initial flow pattern. In all considered geometric configurations, the same steady flow pattern was obtained whatever the initial conditions (symmetric vs. asymmetric), except in the transition zone (i.e.,

221 $S \sim 6.8$) as detailed in section 4.2. This demonstrates that, the computed final steady flow showed
222 some dependency on the initial conditions in the transition zone only, consistently with previous
223 experimental observations (Dufresne et al., 2010b; Camnasio et al., 2011).

224 **4. RESULTS**

225 ***4.1 Flow patterns and velocity profiles***

226 Dufresne et al. (2010b) showed that a symmetric flow pattern is observed for S below 6.2 and an
227 asymmetric flow pattern for S above 6.8. In-between those two thresholds, the flow was reported to
228 be in a transition zone, because it alternately showed a symmetric and an asymmetric pattern for
229 repeated tests in the same conditions. Dufresne et al. (2010b) made no distinction between
230 symmetric flow patterns with (S1) and without (S0) reattachment point.

231 As detailed in Table 1, the experimentally observed flow patterns in the present study agree with the
232 predictions of Dufresne et al. (2010b), except for tests 2 and 3 which are in or close to the transition
233 zone. The later tests lead here to a symmetric flow field with one reattachment point on each side-
234 wall of the reservoir (S1 pattern).

235 The numerical model, based on the depth-averaged k-ε turbulence closure, generally succeeds in
236 reproducing the same flow pattern as in the experiments, except for the S1 pattern. This flow pattern
237 was not reproduced by the numerical model, but S0 flow patterns were predicted instead. In the
238 tested reservoir configurations, the numerical model is thus unable to reproduce the two small and
239 slowly recirculating upstream eddies, which are observed in the experiments. This may result from
240 three-dimensional effects which are not incorporated in the numerical model. Dewals et al. (2008)
241 also highlighted the difficulty of reproducing with a depth-averaged model the small slowly-rotating
242 vortices present in the upstream of the reservoir, such as in flow pattern S1.

243 For four reservoir geometries corresponding to the four different flow patterns (Figure 4),
244 experimentally measured cross-sectional profiles of the longitudinal velocity have been compared

with numerical results (Figure 5). The k-ε model is found to perform relatively well at predicting the width of the main jet and the overall velocity distribution, particularly for test 5 and, for all tests, in the downstream part of the reservoir.

4.2 Mean kinetic energy

To complement local comparisons along cross-sections, the kinetic energy in the reservoir has been used as a global indicator to compare measured and computed velocity fields. The kinetic energy content E_{tot} (m^4/s^2) of the reservoir is defined as the integral over the reservoir surface of the local kinetic energy per unit mass associated to the depth-averaged velocity:

$$E_{tot} = \int_A \frac{1}{2}\left(u^2 + v^2\right) dA \tag{14}$$

with A the reservoir surface (m^2). Integral (14) can be evaluated numerically either from the grid of measured velocity components or from the simulated values in each computational cell. To avoid the dependence of this indicator to the scale of the considered reservoir, the specific energy content $e_{spec} = E_{tot} / A$ (m^2/s^2) has been introduced in this study. This specific energy is further normalized by a reference specific energy e_{ref} to lead to a non-dimensional indicator: $e_{nd} = e_{spec} / e_{ref}$.

The reference specific energy is defined as the specific energy corresponding to an idealized straight jet in the middle of the reservoir:

$$e_{ref} = \frac{1}{2}\left(\frac{Q}{bh}\right)^2 \frac{bL}{BL} = \frac{1}{2}\frac{Q^2}{bBh^2}\,. \tag{15}$$

Consequently, the non-dimensional indicator e_{nd} takes values of the order of unity and would equal unity in the hypothetical case of a flow pattern with zero-velocity in the recirculation zones and no spreading of the jet.

The value of the non-dimensional specific energy content e_{nd} as derived from the velocity measurements is shown in Figure 6 as a function of the shape parameter S represented on a logarithmic axis. The indicator e_{nd} monotonously decreases as the shape parameter increases, which is in qualitative agreement with the higher trapping efficiency reported for reservoirs of shape

parameter higher than the threshold value 6.8 (Dufresne et al., 2010a). In addition, as shown in Figure 6, the values of e_{nd} show a distinctive linear tendency, which can be represented by the following linear relationship between e_{nd} and the logarithm of S:

$$e_{nd} = 1 - \frac{1}{2}\ln\left(\frac{1}{2}\frac{S}{S_{cr}}\right) \quad (16)$$

where $S_{cr} = 6.5$ is the value of the shape parameter at the center of the transition zone, extending from $S = 6.2$ to $S = 6.8$ as defined by Dufresne et al. (2010b).

Although surprisingly simple, relationship (16) could not be predicted nor derived from more theoretical considerations. In contrast, it confirms once again the important role of the shape factor S, based on the definition introduced by Dufresne et al. (2010) and, therefore, the relevance of using this parameter to characterize the influence of the reservoir geometry on the flow characteristics. Indeed, it enables to lump all relevant geometric parameters (L, B, ΔB, b) into one single non-dimensional number, S. Similarly, in another recent investigation, Peltier et al. (2014a; b) also highlighted the ability of the parameter S to reflect the overall influence of the reservoir geometry on the occurrence of meandering flow in such rectangular shallow reservoirs.

Figure 6 reveals that two different flow patterns are obtained for nearly similar values of S slightly higher than S_{cr}, which is consistent with the experimental evidence of co-existence of both flow patterns S0 and A1 within the transition zone (Camnasio et al., 2011; Dufresne et al., 2010b).

Next, a comparison between the measured specific kinetic energy and the numerical predictions is given in Figure 7. The results of the k-ε model agree relatively well with the measurements, as the numerical predictions of the specific kinetic energy lead to a mean relative error of 10% and the relative errors range in-between 3% and 20%.

4.3 Turbulent kinetic energy

The instantaneous horizontal velocity components u and v can be decomposed in the following way: $u = \overline{u} + u'$ and $v = \overline{v} + v'$. $\overline{u}$ and $\overline{v}$ represent time-averaged quantities, while u' and v' are the

fluctuating components of velocity due to turbulence. Neglecting the small contribution which would be given by the vertical velocity fluctuating component *w'*, the turbulent kinetic energy per unit mass *k* can be defined as:

$$k = \frac{1}{2}\left(\overline{u'^2} + \overline{v'^2}\right). \quad (17)$$

The experimental values of *k* were compared to the values of *k'* derived from the *k*-ε numerical model. Since this model provides the depth integrated value $k' \approx k\,h$ (Erpicum et al., 2009), the model output has been simply divided by the water height *h* to obtain the usual form of turbulent kinetic energy *k*.

In Figure 8, the experimental and the numerical profiles of *k* for different cross sections of the four reservoir configurations are shown. Along the main jet, where turbulent kinetic energy takes its maximum values (of the order of 10^{-4} m^2/s^2), the experimental values match reasonably well the turbulence values resulting from the numerical model. On the contrary, the turbulence in the recirculation zones, outside of the main jet, is in general significantly overestimated by the numerical model.

5. DISCUSSION

Besides the depth-averaged *k*-ε model discussed above, a simple algebraic model based on Elder formula (see Equ. (10)-(11)) is another turbulence closure which was also used in previous literature about rectangular shallow reservoirs, particularly for the experimental setup considered here (Dewals et al., 2008; 2012; Dufresne et al., 2011). Therefore, we compare here the results of this algebraic turbulence closure with those of the depth-averaged *k*-ε model.

While the *k*-ε model succeeds in predicting the observed flow patterns in most geometric configurations, the predictions of the algebraic turbulence model show more discrepancies compared to the experiments (Table 1). First, the transitions between the symmetric flow field S0 and the asymmetric flow fields A1 and A2 are shifted, as highlighted by tests n°2 and n°9. Second,

317 this model fails to reproduce the A2 flow pattern observed for high values of the shape parameter
318 and predicts instead a plug flow (tests n°10 and n°11).
319 The cross-sectional velocity profiles are better reproduced by the depth-averaged k-ε model than by
320 the algebraic one, which systematically overestimates the jet diffusion in the reservoir (Figure 5). In
321 particular, the velocity profiles predicted by the algebraic model for the reservoir of 6 m × 0.75 m
322 are almost uniform along the reservoir width (plug flow) for $x \approx 2$ m and above, in contrast with the
323 A2 flow pattern observed experimentally.
324 Similarly, for the mean kinetic energy of the flow, the predictions of the k-ε model agree
325 significantly better with the measurements than those from the algebraic model (Figure 7). Indeed, a
326 significant positive bias is found in the results of the algebraic model, which systematically
327 overestimates the measurements except for the two configurations in which a plug flow is predicted
328 instead of an A2 flow pattern (tests n°10 and 11). The root-mean-square error in the case of the
329 algebraic model (7.2×10^{-4} m^2/s^2) is more than three times higher than for the k-ε model (2.1×10^{-4}
330 m^2/s^2). This confirms the poorer performance of the algebraic model compared to the k-ε model, as
331 highlighted above by the comparisons of velocity fields and cross-sectional profiles.

332 **6. CONCLUSIONS**

333 This paper presents the results of experimental measurements carried out for eleven different
334 configurations of rectangular shallow reservoirs. The expansion ratio and the length-to-width ratio
335 of the reservoir have been varied, whereas the hydraulic conditions were kept constant. The flow
336 fields were measured experimentally throughout the reservoir by means of UVP probes. The
337 observed flow patterns are consistent with the previous findings by Dufresne et al. (2010b)
338 regarding the influence of the reservoir geometry on the flow pattern and the role of the shape
339 factor *S*.

For the first time, the mean kinetic energy content of the flow has been analysed as a function of the geometry of the reservoir. Based on the experimental measurements, a new and simple relationship between the shape factor S and the non-dimensional specific energy content of the flow has been derived: the specific mean kinetic energy, normalized by a reference value, is a linear function of the logarithm of the reservoir shape factor.

We also compare the experimentally measured flow fields to the results of depth-averaged numerical simulations based on a two-length-scale k-ε model. This model succeeds in predicting the observed flow fields fairly accurately, except for small recirculations in the symmetric flow pattern, which are not reproduced. The specific mean kinetic energy of the entire reservoir has also been used as a global indicator to compare measured and simulated flow fields. It confirms the ability of the depth-averaged k-ε model to reproduce the observed mean kinetic energy of the flow.

Next, an algebraic turbulence model has been tested; but it leads to incorrect flow patterns for several geometric configurations and the diffusion of the jet in the computed results is strongly overestimated compared to the measured velocity profiles.

Finally, the k-ε model has been shown to provide satisfactory predictions of the turbulent kinetic energy in the main jet, but it leads to systematic overestimations in the recirculation zones, where an accurate prediction of turbulent diffusion is however essential to predict mixing of suspended sediments and location of deposits.

For future developments, an enhanced calibration of the k-ε model may be necessary to improve these computational results, as well as more advanced turbulence models such as large eddy simulations. The remaining discrepancies may also result from the three-dimensional nature of the flow in the recirculation zones, where secondary currents may be involved. This should be further investigated using a 3D flow model (e.g., Haun et al., 2011; Chau and Jiang, 2001). More advanced experimental techniques for flow visualization should also be applied in order to verify the 2D or 3D nature of the flow fields, particularly as a function of the shape factor.

Similarly, the overall influence of hydraulic conditions on the patterns of velocity, mean kinetic energy and turbulent kinetic energy should be further investigated. This can be achieved by using validated numerical models such as the model presented here. In addition to the geometry, the main hydraulic parameters, such as Reynolds number, Froude number and shallowness of the flow, should be varied systematically to come up with sufficiently generic conclusions.

Finally, simulations predicting the amount and location of sediment deposits should be undertaken based either on standard morphodynamic models relying on a continuous description of the solid phase or on Lagrangian approaches for the solid particles (e.g., Tarpagkou and Pantokratoras, 2013). More research is needed to successfully reflect in these simulations the complex interactions between the mean flow, the turbulence and the convective as well as diffusive transport of sediments (e.g., Mariotti et al., 2013).

NOMENCLATURE

L = Reservoir length (m)

B = Reservoir width (m)

h = Water depth (m)

b = Width of inlet channel (m)

E_{tot} = Kinetic energy content of the reservoir (m^4/s^2)

e_{spec} = Specific energy content of the reservoir (m^2/s^2)

e_{nd} = Non-dimensional indicator of the specific energy content of the reservoir (-)

e_{ref} = Reference specific energy content of the reservoir (m^2/s^2)

$J_{x,y}$ = components of the friction slope along the x and y directions (-)

k = Turbulent kinetic energy per unit mass (m^2/s^2)

k' = Depth-integrated turbulent kinetic energy per unit mass (m^3/s^2)

Fr_{in} = Froude number of the inlet channel (-)

g = Gravitational acceleration (m/s^2)

Q = Discharge (m^3/s)

Re_{in} = Reynolds number of the inlet channel (-)

u = Reynolds-averaged and depth-averaged horizontal velocity component in x direction (m/s)

u' = Fluctuating horizontal velocity component in x direction (m/s)

$\bar{u}$ = Time-averaged velocity component in x direction (m/s)

S = Shape factor (-)

S_{cr} = Shape parameter ate the centre of the transition zone (-)

A = Reservoir surface (m^2)

t = time (s)

u^* = Friction velocity (m/s)

401 v = Reynolds-averaged and depth-averaged horizontal velocity component in x direction (m/s)

402 v' = Fluctuating horizontal velocity component in y direction (m/s)

403 V = Depth-averaged velocity (m/s)

404 V_{in} = Average inlet-channel velocity (m/s)

405 v = Instantaneous horizontal velocity component in y direction (m/s)

406 w' = Fluctuating vertical velocity component in z direction (m/s)

407 x = Longitudinal coordinate along reservoir length (m)

408 y = Transversal coordinate along reservoir width (m)

409 z = Distance along the vertical direction (m)

410 z_b = Elevation of the bottom from a zero reference level (m)

411 α = Empirical coefficient of the algebraic model (-)

412 ν = Eddy viscosity of water (m^2/s)

413 τ = turbulent stress (N/m^2)

414 ΔB = Lateral expansion of the reservoir (m)

415 ρ = Water density (N/m^3)

416 ε = rate of dissipation of turbulent kinetic energy (m^2/s^3)

417

418 **REFERENCES**

419 Camnasio E, Orsi E, Schleiss AJ (2011). Experimental study of velocity fields in rectangular
420 shallow reservoirs. *Journal of Hydraulic Research* 49(3):352-358.

421 Camnasio E, Erpicum S, Orsi E, Pirotton M, Schleiss AJ, Dewals B (2013). Coupling between flow
422 and sediment deposition in rectangular shallow reservoirs. *Journal of Hydraulic Research*
423 51(5):535-547.

424 Babarutsi S, Chu VH (1998). Modeling transverse mixing layer in shallow open-channel flows.
425 *Journal of Hydraulic Engineering - ASCE* 124(7):718-727.

426 Chau KW, Jiang YW (2001). 3D numerical model for Pearl River estuary. *Journal of Hydraulic*
427 *Engineering - ASCE* 127(1):72-82

Chau KW, Jiang YW (2004). A three-dimensional pollutant transport model in orthogonal curvilinear and sigma coordinate system for Pearl river estuary. *International Journal of Environment and Pollution* 21(2):188-198.

Chu VH, Liu F, Altai W (2004). Friction and confinement effects on a shallow recirculating flow. *Journal of Environmental Engineering and Science* 3(5):463-475.

Choi S-U, Garcia M (2002). $k–\varepsilon$ turbulence modelling of density currents developing two dimensionally on a slope. *Journal of Hydraulic Engineering - ASCE* 128(1):55-63.

Dewals BJ, Kantoush SA, Erpicum S, Pirotton M, Schleiss AJ (2008). Experimental and numerical analysis of flow instabilities in rectangular shallow basins. *Environmental Fluid Mechanics* 8(1):31-54.

Dufresne M, Vazquez J, Terfous A, Ghenaim A, Poulet JB (2009). CFD Modeling of Solid Separation in Three Combined Sewer Overflow Chambers. *Journal of Environmental Engineering* 135(9):776-787.

Dufresne M, Dewals BJ, Erpicum S, Archambeau P, Pirotton M (2010a). Experimental investigation of flow pattern and sediment deposition in rectangular shallow reservoirs. *International Journal of Sediment Research* 25(3):258-270.

Dufresne M, Dewals BJ, Erpicum S, Archambeau P, Pirotton M (2010b). Classification of flow patterns in rectangular shallow reservoirs. *Journal of Hydraulic Research* 48(2):197-204.

Dufresne M, Dewals BJ, Erpicum S, Archambeau P, Pirotton M (2011). Numerical investigation of flow patterns in rectangular shallow reservoirs. *Engineering Applications of Computational Fluid Mechanics* 5(2):247-258.

Dufresne M, Dewals B, Erpicum S, Archambeau P, Pirotton M (2012). Flow patterns and sediment deposition in rectangular shallow reservoirs. *Water and Environment Journal* 26(4):504-510.

Erpicum S, Meile T, Dewals BJ, Pirotton M, Schleiss AJ (2009). 2D numerical flow modeling in a macro-rough channel. *International Journal for Numerical Methods in Fluids* 61(11):1227-1246.

Erpicum S, Dewals BJ, Archambeau P, Pirotton M (2010). Dam break flow computation based on an efficient flux vector splitting. *Journal of Computational and Applied Mathematics* 234(7):2143-2151.

Fischer HB, List EJ, Koh RCY, Imberger J, Brooks NH (1979). *Mixing in Inland and Coastal Waters*, Academic Press.

Goula AM, Kostoglou M, Karapantsios TD, Zouboulis AI (2008). A CFD methodology for the design of sedimentation tanks in potable water treatment. Case study: The influence of a feed flow control baffle. *Chemical Engineering Journal* 140(1-3):110-121.

Haun S, Olsen NRB, Feurich R (2011). Numerical Modeling of Flow over Trapezoidal Broad-Crested Weir. *Engineering Applications of Computational Fluid Mechanics* 5(3):397-405.

Lai W, Khan AA (2012). Discontinuous Galerkin Method for 1D Shallow Water Flows in Natural Rivers. *Engineering Applications of Computational Fluid Mechanics* 6(1):74-86.

Lee YH, Kim KW, Kvon A, Kwak MK, Lee CY, Kim GM, Park CW (2013). Experimental investigation of bubbly flow mixing inside a washer basin with an immersed coiled heater. *Applied Mechanics and Materials* 372:387-391.

Liu H, Zhou JG, Shafiai S, Peng Y, Burrows R (2010). Lattice Boltzmann method for open-channel flows. *Proceedings of the ICE - Engineering and Computational Mechanics* 163:243-249.

Mariotti G, Falcini F, Geleynse N, Guala M, Sun T, Fagherazzi S (2013). Sediment eddy diffusivity in meandering turbulent jets: Implications for levee formation at river mouths. *Journal of Geophysical Research. Earth Surf.* 118(3):1908-1920.

Ng W-Y, Chau C-K (2014). A modeling investigation of the impact of street and building configurations on personal air pollutant exposure in isolated deep urban canyons. *Science of the Total Environment* 468-469:429-448.

Peltier Y, Erpicum S, Archambeau P, Pirotton M, Dewals B (2014a). Experimental investigation of meandering jets in shallow reservoirs. *Environmental Fluid Mechanics* 14(3):699-710.

Peltier Y, Erpicum S, Archambeau P, Pirotton M, Dewals B (2014b). Meandering jets in shallow rectangular reservoirs: POD analysis and identification of coherent structures. *Experiments in Fluids* 55:1740.

Peng Y, Zhou J, Burrows R (2011). Modeling Free-Surface Flow in Rectangular Shallow Basins by Using Lattice Boltzmann Method. *Journal of Hydraulic Engineering - ASCE* 137(12):1680-1685.

Roache PJ (1994). Perspective: a method for uniform reporting of grid refinement studies. *Journal of Fluids Engineering, Transactions of the ASME* 116(3):405-413.

Tarpagkou R, Pantokratoras A (2013). CFD methodology for sedimentation tanks: The effect of secondary phase on fluid phase using DPM coupled calculations. *Applied Mathematical Modelling* 37(5):3478-3494.

Wu CL, Chau KW (2006). Mathematical model of water quality rehabilitation with rainwater utilization - a case study at Haigang. *International Journal of Environment and Pollution* 28(3-4):534-545.

FIGURES AND TABLES

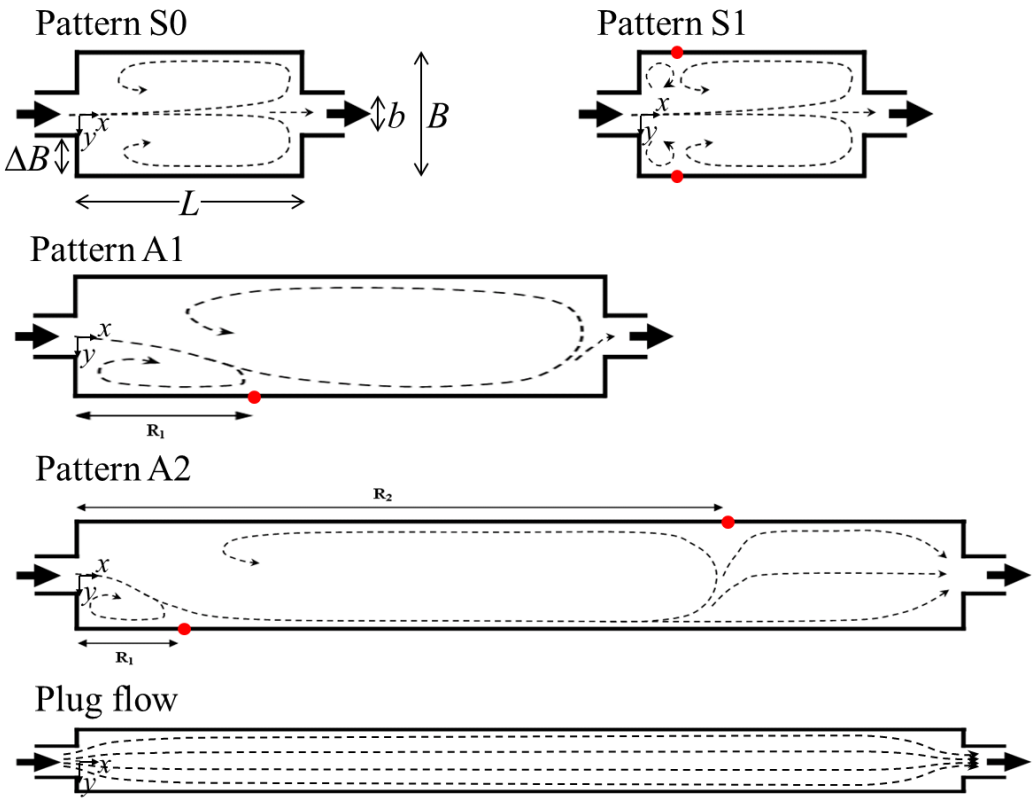

Figure 1: Main flow patterns observed in shallow rectangular reservoirs: the flow shows zero, one or two reattachment points (•) depending on the reservoir geometry. Adapted from Dufresne et al. (2012).

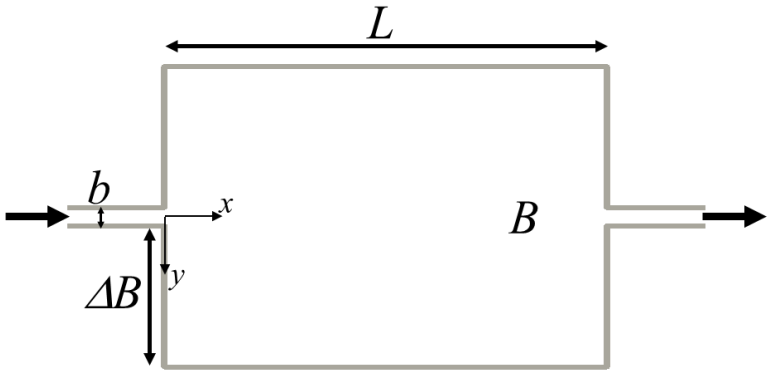

Figure 2: Sketch of the experimental reservoir and definition of main geometric notations.

503

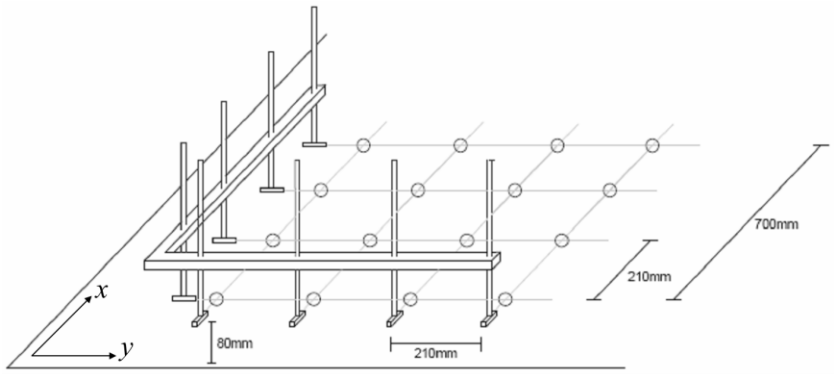

504 Figure 3: Setup of eight UVP devices to enable two-component velocity measurements at sixteen
505 different points in the flow (○).

506

507

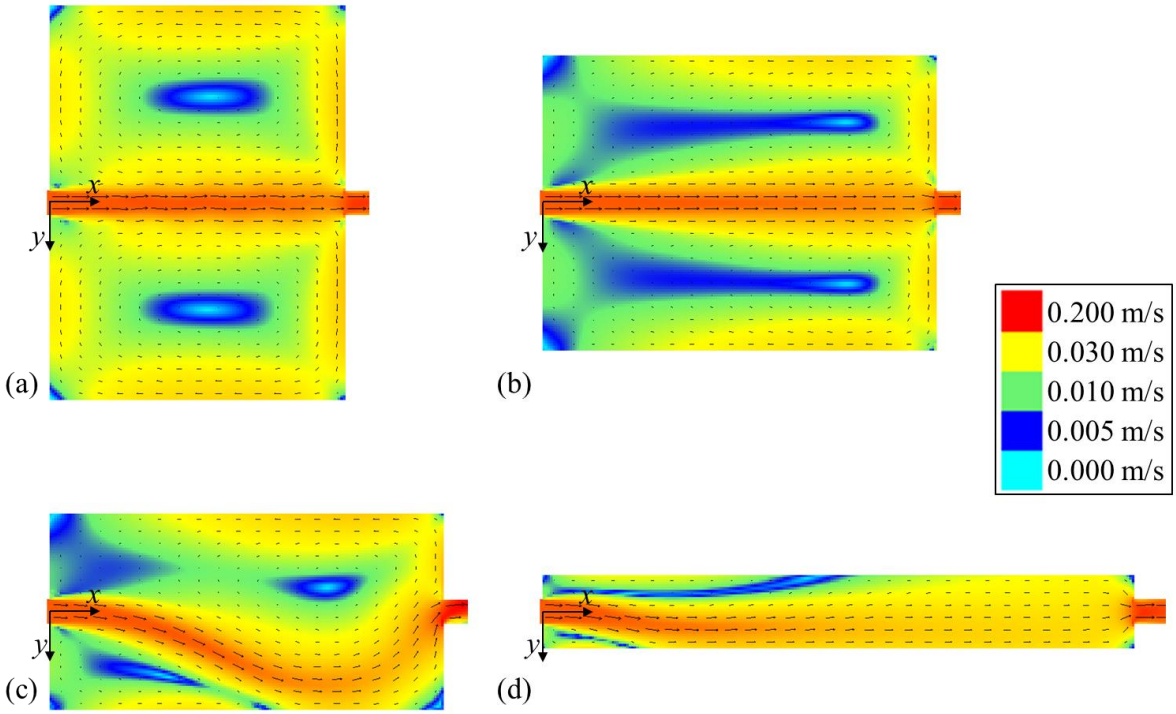

508 Figure 4: Flow fields computed in four reservoir geometries using the depth-averaged k-ε model:
509 (a) Test 5, (b) Test 6, (c) Test 7 and (d) Test 10.

510

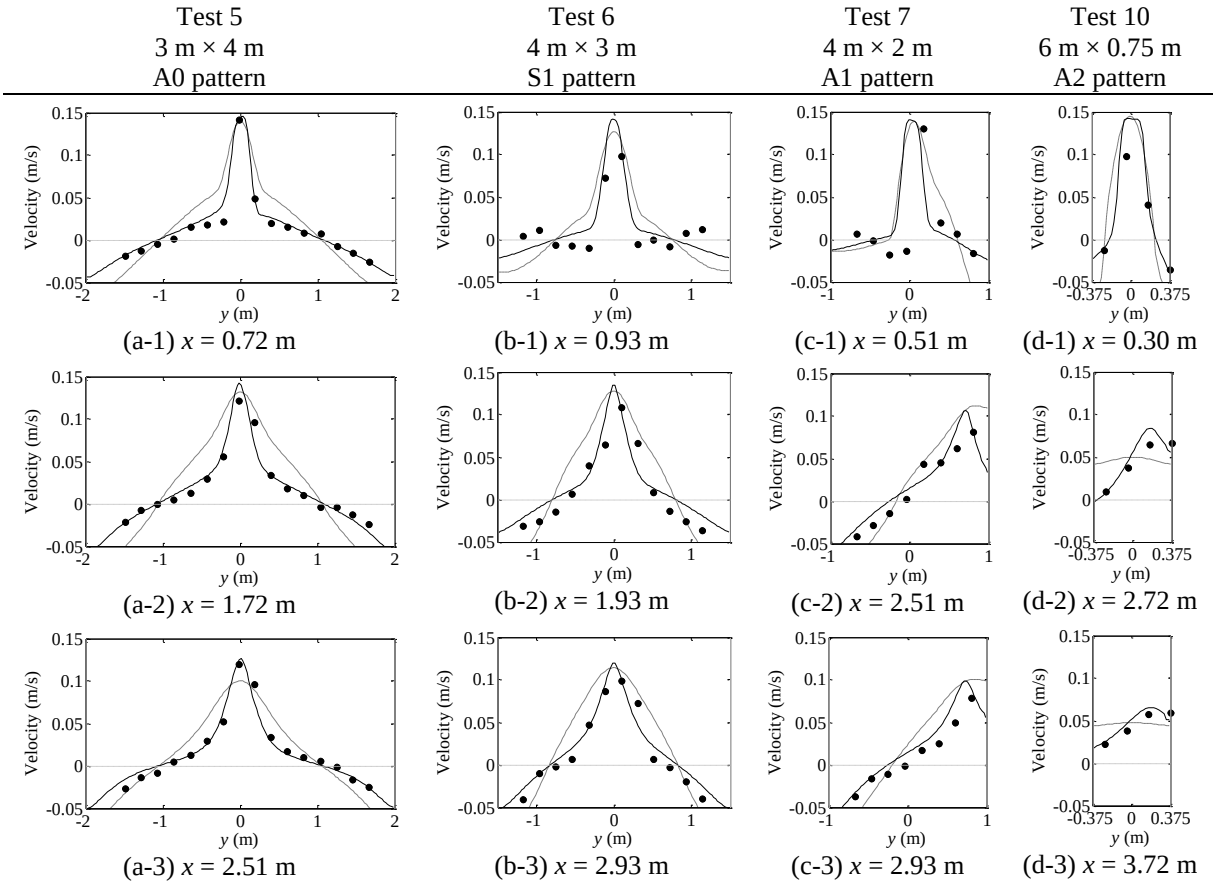

Figure 5: Observed and computed cross-sectional velocity profiles for the four reservoir geometries corresponding to tests 5, 6, 7 and 10: experimental (●) and simulated with the k-ε model (——) and with the algebraic turbulence model (– – –).

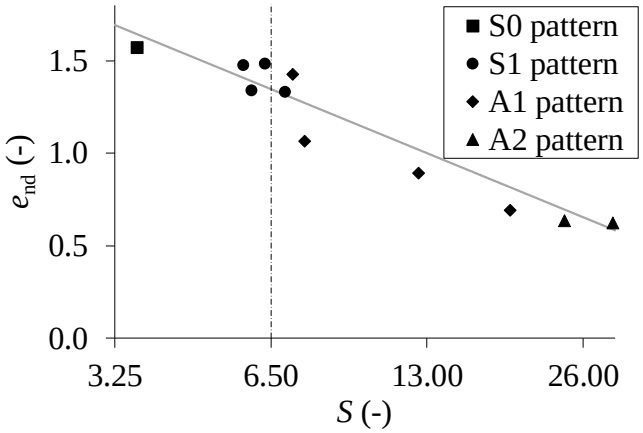

Figure 6: The non-dimensional specific energy content derived from velocity measurements varies linearly with the logarithm of the shape factor $S = L / \Delta B^{0.6} / b^{0.4}$.

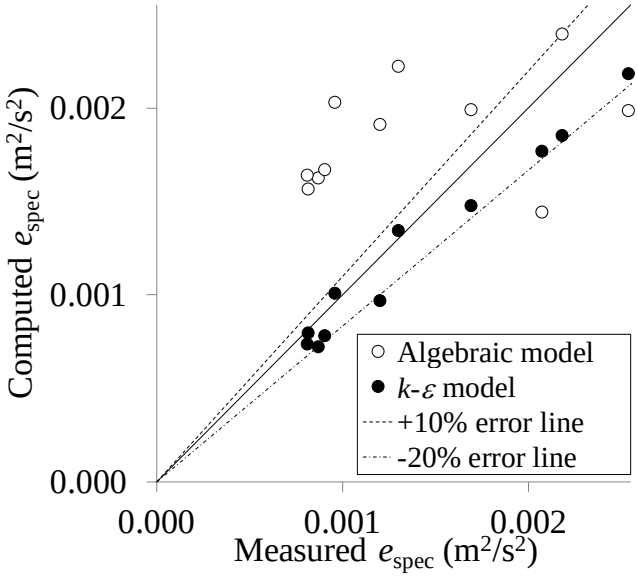

521

522 Figure 7: Compared to the algebraic turbulence model, the k-ε model leads to more accurate
523 predictions of the specific kinetic energy content e_{spec}.
524
525

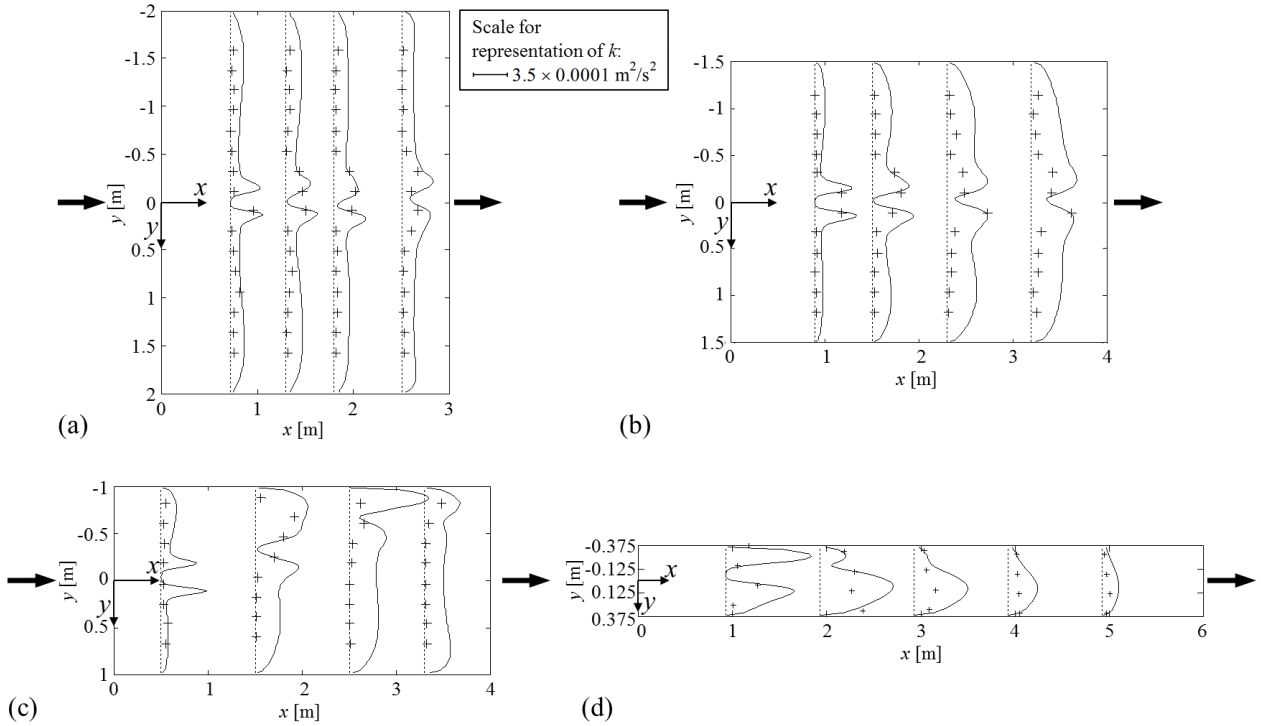

526

527 Figure 8: Comparison between measured (+) and computed (——) turbulent kinetic energy k for the
528 different types of flow patterns: (a) L = 3 m, B = 4 m, pattern S1; (b) L = 4 m, B = 3 m, pattern S0;
529 (c) L = 4 m, B = 2 m, flow pattern A1; (d) L = 6 m, B = 0.75 m, flow pattern A2. The dashed lines
530 locate each cross-section for which comparisons are presented and they also indicate the zero level
531 for the corresponding representation of turbulent kinetic energy.
532

533 Table 1: Length L, width B, non-dimensional length L / ΔB, expansion ratio ΔB / b, shape parameter
534 $S = L / \Delta B^{0.6} / b^{0.4}$ as well as observed and simulated flow patterns in the considered geometric
535 configurations.

Test ID	L (m)	B (m)	L / ΔB (-)	ΔB / b (-)	S (-)	Flow patterns		
						Observed	k-ε model	Alg. mod.
1	6	4	3.2	7.5	7.2	A1	A1	A1
2	5.8	4	3.1	7.5	6.9	S1	S0	A1
3	5.3	4	2.8	7.5	6.3	S1	S0	S0
4	5	4	2.7	7.5	6.0	S1	S0	S0
5	3	4	1.6	7.5	3.6	S0	S0	S0
6	4	3	2.9	5.5	5.8	S1	S0	S0
7	4	2	4.6	3.5	7.5	A1	A1	A1
8	4	1	10.7	1.5	12.5	A1	A1	A1
9	6	1	16.0	1.5	18.8	A1	A1	A2
10	6	0.75	24.0	1	24.0	A2	A2	Plug flow
11	6	0.6	34.3	0.7	29.7	A2	A2	Plug flow

536

537

538